Hidden Symmetry in Interacting-Quantum-Dot-Based Multiterminal Josephson Junctions

Peter Zalom,[1,*] M. Žonda,[2,†] and T. Novotný[2,‡]
[1]Institute of Physics, Czech Academy of Sciences, Na Slovance 2, CZ-18200 Praha 8, Czech Republic
[2]Department of Condensed Matter Physics, Faculty of Mathematics and Physics, Charles University, Ke Karlovu 5, CZ-121 16 Praha 2, Czech Republic

(Received 20 October 2023; accepted 21 February 2024; published 21 March 2024)

We study a multiterminal Josephson junction based on an interacting quantum dot coupled to n superconducting BCS leads. Using an Anderson type model of a local level with an arbitrary on-site Coulomb repulsion, we uncover its surprising equivalence with an effective two-terminal junction with symmetric couplings to appropriately phase-biased leads. Regardless of the strength of the Coulomb interaction, this hidden symmetry enables us to apply well-established numerical and theoretical tools for exact evaluation of various physical quantities, and imposes strict relations among them. Focusing on three-terminal devices, we then demonstrate several phenomena such as the existence of the finite energy band crossings and superconducting transistor and diode effects, as well as current phase relation modulation.

DOI: 10.1103/PhysRevLett.132.126505

Introduction.—Josephson junctions (JJs) serve as fundamental components for a range of quantum devices thanks to their precise superconducting phase control [1–5]. Therefore, their multiterminal counterparts with $n \geq 3$ leads have recently received significant theoretical attention. From a topological perspective, their subgap energy levels span a synthetic $(n-1)$-dimensional Brillouin zone (BZ) leading to the potential emergence of zero- and finite-energy Weyl nodes [6–13]. Additionally, multiterminal JJs with integrated topological superconductors hold promise for performing braiding operations on zero-energy Majorana bound states [14,15], while in the nonequilibrium regime, intriguing phenomena such as Cooper pair quartet transport emerge [16]. On the experimental front, the realization of multiterminal superconducting (SC) devices has recently advanced significantly, with pioneering experiments in graphene [17], weak links [18], and ongoing innovations appearing [19–24].

Because of the computational constraints arising from the number of leads, interactions within the central junction region are mostly neglected or approximated [25–27]. Notably, even the numerical renormalization group (NRG), a standard for analyzing strongly interacting superconducting single-level Anderson impurity models (SC-AIM), whose relevance to accurately describe realistic experimental setups was established over a decade ago [28,29], faces challenges in this context [30].

In this Letter, we show that the paradigmatic n-terminal SC-AIM can be *exactly* mapped onto a two-terminal version with symmetric tunnel couplings and a suitable phase bias. The mapping is completely determined by the original configuration through a gauge-invariant geometric factor denoted as χ. Since the two-terminal SC-AIM can be exactly addressed by means of NRG [30–34] and quantum Monte Carlo [29,35–37], or by other numerous tools [25–27,38–40], the knowledge of the geometric factor χ can be used to completely understand the behavior of multiterminal SC-AIM as demonstrated here.

Unveiling the geometric properties of the solution for multiterminal SC-AIM allows us to make meaningful and nontrivial assertions about its phase diagrams and associated Josephson currents. We especially highlight the practical possibility to realize the high-symmetry points, which are related to the so-called doublet chimney [40–42] and remain robust regardless of the strength of the Coulomb interaction. Furthermore, our work showcases the practical advantages of incorporating three-terminal quantum dot-based devices into SC circuits, as they introduce SC transistor and diode effects, and enable the modulation of supercurrent phases [43].

Model.—We consider a general multiterminal SC-AIM with a single-level quantum dot (QD) as depicted schematically in Fig. 1(a). Its Hamiltonian reads

$$H = H_d + \sum_{j=1}^{n} (H_{j,\mathrm{SC}} + H_{j,T}), \tag{1a}$$

with $j \in \{1, \ldots n\}$ denoting a given lead with an SC phase φ_j and

$$H_d = \sum_{\sigma} \varepsilon_d d_\sigma^\dagger d_\sigma + U d_\uparrow^\dagger d_\uparrow d_\downarrow^\dagger d_\downarrow, \tag{1b}$$

$$H_{j,\mathrm{SC}} = \sum_{\mathbf{k}\sigma} \varepsilon_{\mathbf{k}j} c_{\mathbf{k}j\sigma}^\dagger c_{\mathbf{k}j\sigma} - \sum_{\mathbf{k}} \left(\Delta_j c_{\mathbf{k}j\uparrow}^\dagger c_{-\mathbf{k}j\downarrow}^\dagger + \mathrm{H.c.} \right), \tag{1c}$$

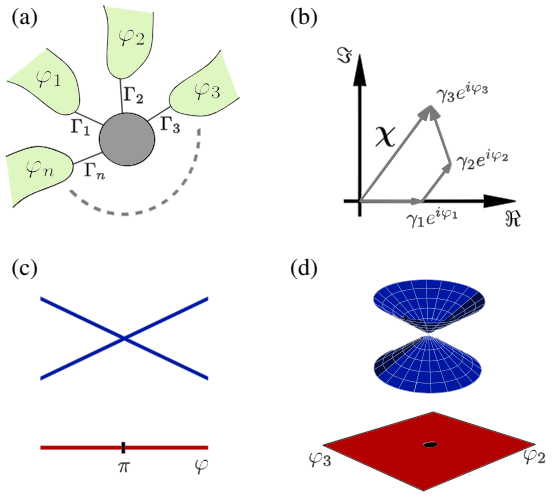

FIG. 1. (a) Schematic depiction of a multiterminal Josephson junction with n SC leads (green) and a centrally placed interacting region of a single level QD (gray). (b) The complex number χ, according to Eq. (3), (shown for $n = 3$) plays a fundamental role for properties of n-terminal SC-AIMs. When $\chi = 0$ finite energy crossings of two singlet states (blue) above a doublet ground state (red) are observed. (c) Singlet crossing for $n = 2$ occurs only under the highly restrictive condition $\Gamma_1 = \Gamma_2$ at $\varphi \equiv \varphi_2 - \varphi_1 = \pi$. (d) For $n = 3$, the singlet crossings appear for $\Gamma_1, \Gamma_2, \Gamma_3$, satisfying a triangular inequality $\gamma_{\max} \leq 1/2$ where $\gamma_{\max} = \max(\{\gamma_j\})$ and $\gamma_j \equiv \Gamma_j / \sum_l \Gamma_l$.

$$H_{j,T} = \sum_{\mathbf{k}\sigma} \left(V^*_{\mathbf{k}j} c^\dagger_{\mathbf{k}j\sigma} d_\sigma + V_{\mathbf{k}j} d^\dagger_\sigma c_{\mathbf{k}j\sigma} \right), \tag{1d}$$

where $c^\dagger_{\mathbf{k}j\sigma}$ ($c_{\mathbf{k}j\sigma}$) creates (annihilates) an electron of spin $\sigma \in \{\uparrow, \downarrow\}$, quasimomentum $\mathbf{k}$, and energy $\varepsilon_{\mathbf{k}j}$ in the lead j, while $d^\dagger_\sigma$ (d_σ) creates (annihilates) a dot electron of spin σ. We assume the same gap Δ and the same band width $2B$ in all leads, so that $\Delta_j \equiv \Delta e^{i\varphi_j}$. Such a choice reflects typical experimental setups, where the terminals are made from the same superconducting material. The coupling to the leads is conveniently characterized by the tunneling strengths ($\hbar = 1$) $\Gamma_j \equiv \pi \sum_{\mathbf{k}} |V_{\mathbf{k}j}|^2 \delta(\omega - \varepsilon_{\mathbf{k}j})$, which are presumed to be energy independent for simplicity. The total tunneling strength is $\Gamma \equiv \sum_{j=1}^n \Gamma_j$, while relative couplings are $\gamma_j \equiv \Gamma_j / \Gamma$ ($\sum_{j=1}^n \gamma_j = 1$). The QD is characterized by its energy level ε_d and Coulomb repulsion U. In this Letter, we focus on a half-filled QD by setting $\varepsilon_d = -U/2$, but stress that all of the findings can be easily extended beyond such a constraint.

Gauge invariance of the solution.—When focusing only on physical quantities related to the dot degrees of freedom, like the on-dot spectral function or thermodynamic quantities such as the free energy and supercurrents, only the dot Green function is required. It is a functional of U and the noninteracting Green function, which, in turn, is a functional of the (retarded) tunneling self-energy $\sum\!\!\!\!\!\!\sum(\omega^+)$ given by the n leads. Using Nambu spinors $D^\dagger = \left(d^\dagger_\uparrow, d_\downarrow\right)$, the matrix form of $\sum\!\!\!\!\!\!\sum(\omega^+)$ becomes

$$\sum\!\!\!\!\!\!\sum(\omega^+) = \Gamma \begin{pmatrix} \omega & \chi\Delta \\ \chi^*\Delta & \omega \end{pmatrix} F(\omega^+), \tag{2}$$

where $F(\omega^+)$ parametrically depends only on Δ and B [see, e.g., Ref. [44] and the Supplemental Material (SM) [45]]. Complex-valued χ reads

$$\chi \equiv \sum_{j=1}^n \gamma_j e^{i\varphi_j} \tag{3}$$

and contains complete information about the geometric configuration of the n-terminal SC-AIM including all relative weights and phase biases. Using the global gauge invariance, we can moreover shift all phases as $\varphi_j \to \varphi_j - \delta$, which rotates χ clockwise by δ, but leaves all physical properties invariant [51]. Consequently, only the gauge-invariant magnitude $\chi \equiv |\chi|$ is of significance, so the replacement $\chi \to \chi$ can be readily performed in Eq. (2). As shown in SM [45], χ can be simplified to

$$\chi \equiv |\chi| = \sqrt{1 - 4 \sum_{j>l=1}^n \gamma_j \gamma_l \sin^2 \frac{\varphi_j - \varphi_l}{2}}. \tag{4}$$

While generally $0 \leq \chi \leq 1$, for $n = 1$ it trivially reads $\chi = 1$. However, already a coupling-symmetric two-terminal SC-AIM encompasses all possible values of χ as $\chi = |\cos(\varphi/2)|$ [52]. Consequently, *any* n-terminal setup can be mapped onto its coupling-symmetric two-lead counterpart with the same U, total Γ and a phase difference φ that corresponds to the multiterminal value of χ. This constitutes the main finding of our work with a number of conceptual and practical implications, which we will explore in what follows.

Before proceeding with the single QD case, we note that our approach can be straightforwardly extended to systems with p dots (levels), of which q ones are connected exclusively to a distinct set of SC leads. These configurations, detailed in SM [45], can be equivalently represented by a mapping where each dot symmetrically couples to just two SC leads. The state of the system is then fully characterized by p total couplings Γ_i at each dot, q real-valued geometric factors χ_i and $q - 1$ local phase shifts δ_i. However, the method breaks down when even a single lead couples to multiple dots (levels).

Phase diagrams.—The introduced mapping reduces the solution of any single level n-terminal setup to that of the corresponding symmetric two-terminal configuration. Consequently, the ground state (GS) of an n-terminal SC-AIM is restricted to either singlet or doublet parity with a quantum phase transition (QPT) occurring at specific

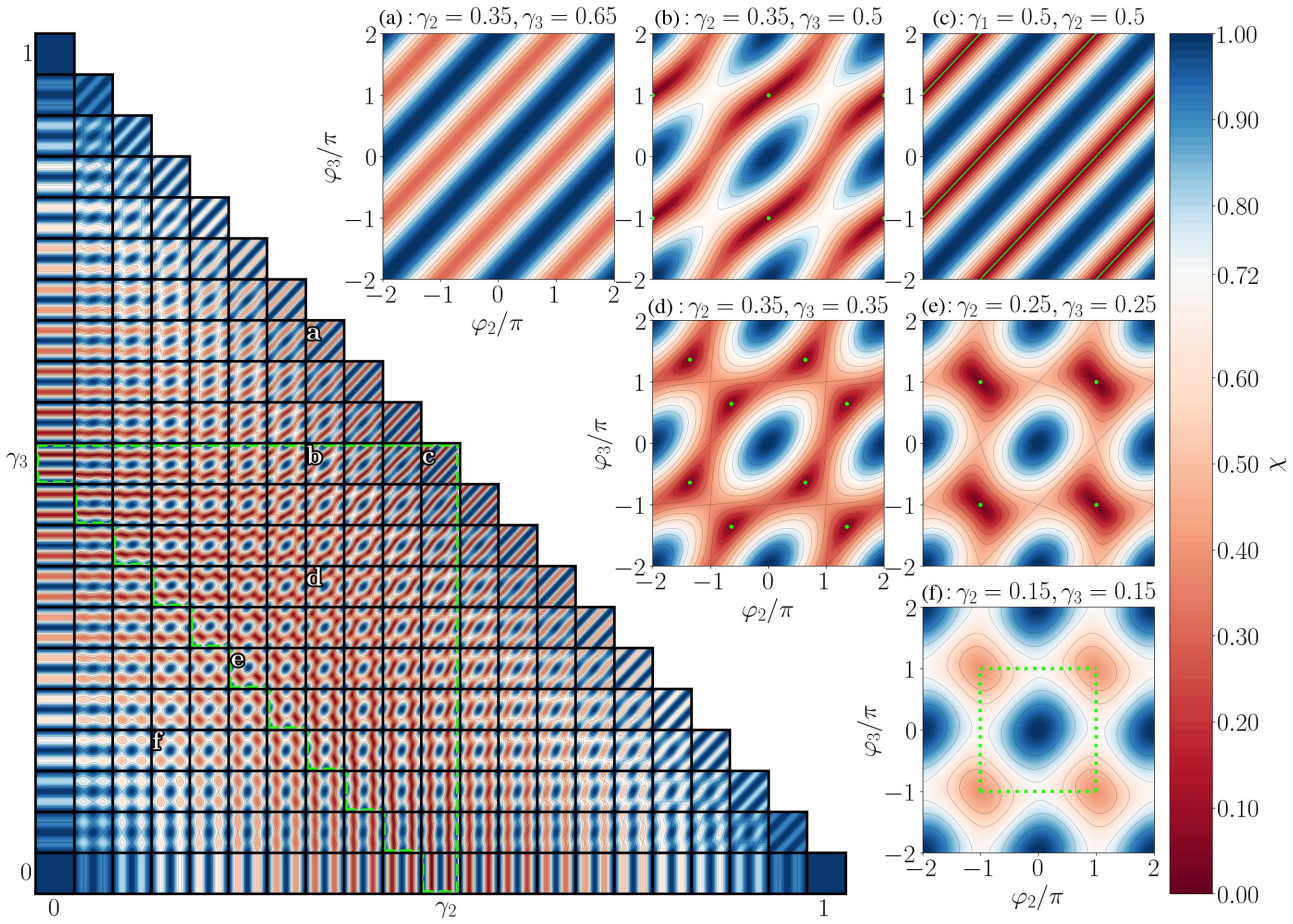

FIG. 2. Maps of geometric factor χ [Eq. (4)] in φ_2—φ_3 planes for a three-terminal setup ($\varphi_1 \equiv 0$) and different values of γ_2 and γ_3. The coloring is chosen so that the maps can be read as phase diagrams for the case $\Gamma = \Delta$, $U = 3\Delta$ for which $\chi^* = 0.721$. Here, white represents the phase boundaries $\chi = \chi^*$, blue marks the singlet GS ($\chi > \chi^*$), and red a doublet GS ($\chi < \chi^*$). In the composite map on the left, the phase diagrams are ordered along the γ_2 and γ_3 axes with a step in γ_2 and γ_3 being 0.05. The maps within the dashed green border satisfy the triangular rule $\max(\{\gamma_j\}) \leq 1/2$ and can therefore host the high-symmetry points, where $\chi = 0$. Four of such cases, e.g., (b)–(e), are shown enlarged with $\chi = 0$ points indicated by green dots [(b), (d), (e)] or solid lines [(c)]. Cases (a) and (f) are taken from the outside of the triangular region. Note that, for clarity, all maps extend beyond the first Brillouin zone, i.e., $\varphi_2, \varphi_3 \in \langle -\pi, \pi \rangle$, which is marked by a dotted green square in panel (f).

critical values χ^* fixed only by the combination of U, Γ, and Δ [5]. The phase diagram therefore turns out to be a contour plot of χ that designates a singlet GS for $\chi > \chi^*$ and a doublet for $\chi < \chi^*$.

For instance, when we select $n = 3$ with $U = 3\Delta$, $\varepsilon_d = -U/2$, and $\Gamma = \Delta$, the QPT point of the corresponding symmetric two-terminal setup, as determined by NRG, is $\chi^* = \cos\varphi^*/2 \approx 0.721$ [see SM [45] and Fig. 3(a)]. Setting now $\varphi_1 = 0$, by virtue of gauge invariance, phase diagrams in the $\varphi_2 - \varphi_3$ plane are obtained by contour plotting χ as shown for varying γ_2 and γ_3 in Fig. 2 in the left triangular map with six particular cases labeled (a) to (f) highlighted on its right. The critical value of χ^* is denoted in white and marks the boundary between the singlet (blue) and doublet (red) GS regions.

Notably, (a) and (c) correspond to the two-terminal setup with a single independent phase difference, as one of the leads is disconnected. The $\varphi_2 - \varphi_3$ maps contain then redundant information in the form of perfect stripes of equivalued χ. Adding a third weakly coupled terminal, initially only bends the parity transition lines as showcased in the inset (b). Moving toward the center of the left triangle map, the bending intensifies, giving rise to isolated pockets of singlet GS in the middle of the phase diagrams, while remnants of the doublet stripes remain as seen in (d). A further increase of γ_1 leads then to the breakdown of the doublet GS stripes, transforming them into four doublet GS pockets at the corners of the first BZ, as depicted in (e) and (f).

In the end, the universal nature of the χ factor in determining phase diagrams cannot be understated, as changing U and Γ requires just replotting of the above color maps by using the respective χ^*. On the other hand, when n is altered, one updates only the geometric factor χ,

but χ^* remains the same (see SM [45] for examples of $n = 4$).

High-symmetry points.—When $\chi = 0$, a special high-symmetry point appears at $\varepsilon_d = -U/2$. Here, the doublet GS and a finite energy crossing of two excited singlets is protected by an additional symmetry in the spin space of the QD for an arbitrary number of terminals [53] as illustrated for $n = 2$ in Fig. 1(c) and for $n = 3$ in Fig. 1(d). Recently, it has gained a lot of attention since it relates to the so-called doublet chimney in the phase diagram of the two-terminal setup [40–42]. However, it is crucial to note that in the two-terminal setup, this high-symmetry point can only be realized under perfectly symmetric coupling conditions. Consequently, its experimental realization remains a formidable challenge, primarily due to the limited control over coupling strengths during device fabrication, although the doublet chimney related to the symmetry of this point is far more robust and was already realized experimentally in Ref. [41].

Nevertheless, in multiterminal setups the realization of high-symmetry points is more straightforward, as can be deduced from Fig. 1(b). To obtain $\chi = 0$, a closed loop, which begins and ends in zero, needs to be formed when summing $\gamma_j e^{i\varphi_j}$ contributions together. Clearly, the task simplifies as n increases. Already for $n = 3$, the solution for the phases reads

$$\varphi_j^{\pm} = \pi \mp (-1)^j \arccos \frac{1 - 2(\gamma_2 + \gamma_3 - \gamma_2\gamma_3 + \gamma_j^2)}{2(1 - \gamma_2 - \gamma_3)\gamma_j} + 2\pi z_j, \tag{5}$$

with $j \in 2, 3$ ($\varphi_1 \equiv 0$) and $z_j \in \mathbb{Z}$, $\varphi_3 = \varphi_2 \pm \pi$ for $\gamma_2 = \gamma_3 = 1/2$ and $\varphi_j = \pm\pi$ for $\gamma_1 = \gamma_j = 1/2$. Solution for $\chi = 0$ thus exists, when $\gamma_{\max} \leq 1/2$ where $\gamma_{\max} = \max(\{\gamma_j\})$. This defines a triangular region in the $\gamma_2 - \gamma_3$ coupling space, as highlighted by the green dashed lines in Fig. 2. There are thus no $\chi = 0$ points outside of this region [insets (a) and (f)], but within it pairs of them appear in the first BZ [inset (d)]. Exactly at the border, the pairs merge together, so the number of $\chi = 0$ points reduces to one per the first BZ as seen by moving from (d) to (e) [54]. In clear contrast to the two-terminal setup, one fourth of the parameter space can be tuned into the desired $\chi = 0$ regime, which paves the way for the experimental observation of these special points. Additionally, the symmetry enforces crossing of two excited singlets at finite energy, and their overall behavior for $n = 3$ is described by a two-dimensional Weyl Hamiltonian [Fig. 1(d)]. As explained in SM [45], for $n = 4$, lines or loops of $\chi = 0$ points form in the three-dimensional synthetic BZ with isolated points appearing only for $\max(\{\gamma_j\}) = 1/2$.

Josephson currents.—The versatility of multiterminal Josephson junctions arises from their ability to divide supercurrents into $n \geq 3$ terminals, each denoted as J_j and passing through the respective lead j, as depicted in Fig. 3(b). Diverse novel phenomena unfold then, encompassing SC transistor and SC diode effects, as well as current modulation. To demonstrate these, we apply the Hellmann-Feynman theorem at zero temperature in conjunction with the herein discovered mapping (see also SM [45]):

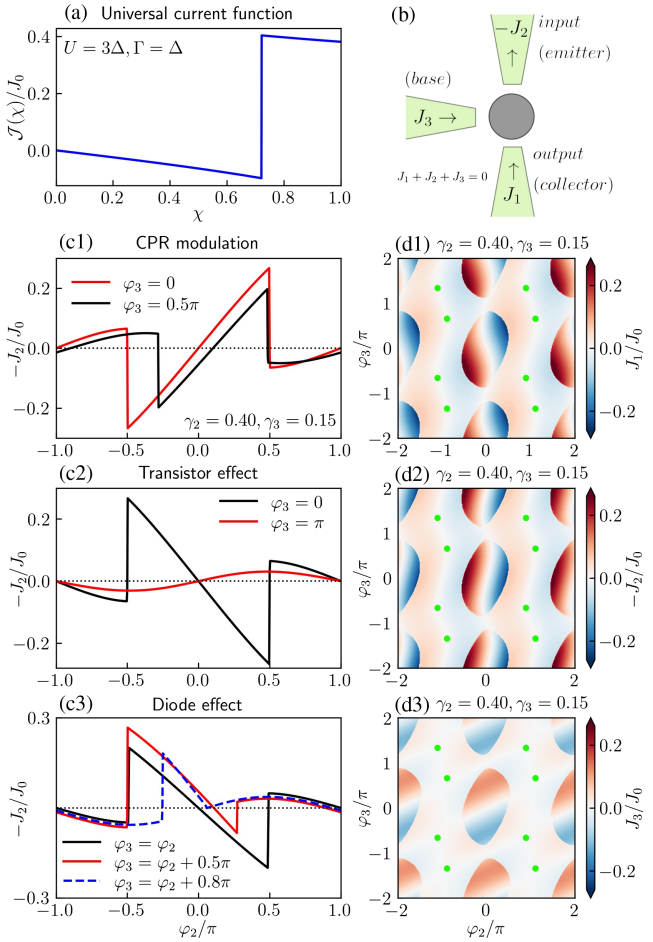

FIG. 3. (a) The universal function $\mathcal{J}(\chi)$ calculated for $U = 3\Delta$ and $\Gamma = \Delta$ and scaled by $J_0 = 2\Delta e/\hbar$. (b) Scheme of the supercurrents J_j in a three-terminal device. (c1) The current phase relation (CPR) of the supercurrent J_2 is modulated by controlling φ_3. (c2) Supercurrent J_2 can be switched off by phase manipulation of the weakly coupled lead $j = 3$, which demonstrates a superconducting transistorlike effect. (c3) J_2 as a function of φ_2 for $\varphi_3 = \varphi_2 + \phi$ illustrates the appearance of a diode effect. Maps (d1), (d2), (d3) show supercurrents J_1, J_2, and J_3 in the $\varphi_2 - \varphi_3$ plane, which correspond to the panels (c1)–(c3). All panels have been obtained for $\gamma_1 = 0.45$, $\gamma_2 = 0.40$, and $\gamma_3 = 0.15$ with $U = 3\Delta$, $\Gamma = \Delta$, and $\varphi_1 \equiv 0$.

$$J_j = \frac{2e}{\hbar}\frac{\partial E}{\partial \varphi_j} = \frac{2e}{\hbar}\frac{\partial E}{\partial \chi}\frac{\partial \chi}{\partial \varphi_j} = \mathcal{J}(\chi)\frac{\partial \chi}{\partial \varphi_j}, \tag{6}$$

where E is the GS energy, $\mathcal{J}(\chi) \equiv (2e/\hbar)(\partial E/\partial \chi)$ is a universal function of χ with parametric dependency on U and Γ, while all geometric details, i.e., n, γ_j, and φ_j, are

confined only to the analytic factors $(\partial\chi/\partial\varphi_j)$. Again, the $\mathcal{J}(\chi)$ input can be extracted from the symmetric two-terminal configuration by a numeric method of choice (for details see SM [45]), with an NRG solution shown in Fig. 3(a) for $U = 3\Delta$ and $\Gamma = \Delta$.

Using $\mathcal{J}(\chi)$ from Fig. 3(a), we select $\gamma_1 = 0.45$, $\gamma_2 = 0.40$, and $\gamma_3 = 0.15$, and determine the corresponding currents J_j in the $\varphi_2 - \varphi_3$ plane ($\varphi_1 \equiv 0$) as plotted in Figs. 3(d1)–3(d3). Notably, QPTs appear congruently at ellipticlike lines dividing positive and negative values of J_j. When changing n, only the $(\partial\chi/\partial\varphi_j)$ function is updated, so the current is replotted correspondingly. $\mathcal{J}(\chi)$ has to be recalculated only if U and/or Γ are changed.

The parameters of resulting device allow treating the third terminal as its base, while J_1 and $-J_2$ are assigned to represent the input and output current, respectively. The selected signs reflect their directions according to Fig. 3(b). Keeping first $\varphi_3 = 0$, the resulting current phase relation (CPR) of $-J_2$, shown in Fig. 3(c1), exhibits nodes at $\varphi_2 = 0, \pi$ in the first BZ and additional QPT points coinciding with the ellipticlike transition lines of Fig. 3(d2). Increasing φ_3 up to $\pi/2$, the CPR is only modulated in phase (the nodes shift) and amplitude. Finally, setting $\varphi_3 = \pi$ forces the device to reside exclusively in the singlet GS, which significantly suppresses $-J_2$, as seen in Fig. 3(c2). This effectively switches off the three-terminal device, akin to a SC-transistor effect.

More elaborate phase control is possible by sweeping φ_2 and simultaneously adjusting $\varphi_3 = \varphi_2 + \phi$. For $\phi = \pi/2$, as depicted in Fig. 3(c3), the CPR is then tuned into a directional regime with different positive and negative critical currents. This results in a SC-diode effect with a yield of ≈50%. We emphasize that CPR modulation and diode effect are quite ubiquitous, while demonstrating the transistor effect required a weakly coupled third terminal and closed pockets of doublet GS pockets that form only at $\gamma_3 \approx 0.15$.

Conclusions.—In this Letter, we explore n-terminal JJs based on a single-level interacting quantum dot described via SC-AIM. Our key insight is their analytic mapping onto two-terminal junctions with symmetric couplings and phase difference expressed via a single analytic quantity χ. This facilitates the derivation of complete phase diagrams and associated Josephson currents, requiring only universal values of critical χ^* and the function $\mathcal{J}(\chi)$, respectively. Geometric details, including the number of leads, SC phases φ_j, and the distribution of total tunneling strength Γ among the leads, are then fully encoded through analytic functions. Importantly, our system supports high-symmetry points, where doublet GS and finite energy band crossing are protected, within a substantial region of experimentally well-accessible coupling space unlike its two-terminal counterpart. In addition, our research emphasizes the practical advantages of integrating three-terminal quantum dot-based devices into Josephson junction circuits to leverage their transistor or diode effects.

The authors would like to thank Virgil V. Baran, Wolfgang Belzig, Jens Paaske, and Rok Žitko for helpful discussions. This work was supported by Grant No. 23-05263K of the Czech Science Foundation and the project e-INFRA CZ (ID:90140) of the Czech Ministry of Education, Youth, and Sports.

*zalomp@fzu.cz
†martin.zonda@matfyz.cuni.cz
‡tomas.novotny@matfyz.cuni.cz

[1] K. Likharev and V. Semenov, IEEE Trans. Appl. Supercond. **1**, 3 (1991).
[2] J. P. Cleuziou, W. Wernsdorfer, V. Bouchiat, T. Ondarcuhu, and M. Monthioux, Nat. Nanotechnol. **1**, 53 (2006).
[3] J. Clarke and F. K. Wilhelm, Nature (London) **453**, 1031 (2008).
[4] A. Martín-Rodero and A. Levy Yeyati, Adv. Phys. **60**, 899 (2011).
[5] V. Meden, J. Phys. Condens. Matter **31**, 163001 (2019).
[6] B. van Heck, S. Mi, and A. R. Akhmerov, Phys. Rev. B **90**, 155450 (2014).
[7] R.-P. Riwar, M. Houzet, J. S. Meyer, and Y. V. Nazarov, Nat. Commun. **7**, 11167 (2016).
[8] E. Eriksson, R.-P. Riwar, M. Houzet, J. S. Meyer, and Y. V. Nazarov, Phys. Rev. B **95**, 075417 (2017).
[9] R. M. Lutchyn, E. P. A. M. Bakkers, L. P. Kouwenhoven, P. Krogstrup, C. M. Marcus, and Y. Oreg, Nat. Rev. Mater. **3**, 52 (2018).
[10] H.-Y. Xie, M. G. Vavilov, and A. Levchenko, Phys. Rev. B **97**, 035443 (2018).
[11] H.-Y. Xie and A. Levchenko, Phys. Rev. B **99**, 094519 (2019).
[12] E. V. Repin and Y. V. Nazarov, Phys. Rev. B **105**, L041405 (2022).
[13] L. P. Gavensky, G. Usaj, and C. A. Balseiro, Europhys. Lett. **141**, 36001 (2023).
[14] J. Alicea, Y. Oreg, G. Refael, F. von Oppen, and M. P. A. Fisher, Nat. Phys. **7**, 412 (2011).
[15] A. Zazunov, R. Egger, M. Alvarado, and A. L. Yeyati, Phys. Rev. B **96**, 024516 (2017).
[16] A. Freyn, B. Douçot, D. Feinberg, and R. Mélin, Phys. Rev. Lett. **106**, 257005 (2011).
[17] A. W. Draelos, M.-T. Wei, A. Seredinski, H. Li, Y. Mehta, K. Watanabe, T. Taniguchi, I. V. Borzenets, F. Amet, and G. Finkelstein, Nano Lett. **19**, 1039 (2019).
[18] N. Pankratova, H. Lee, R. Kuzmin, K. Wickramasinghe, W. Mayer, J. Yuan, M. G. Vavilov, J. Shabani, and V. E. Manucharyan, Phys. Rev. X **10**, 031051 (2020).
[19] G. V. Graziano, M. Gupta, M. Pendharkar, J. T. Dong, C. P. Dempsey, C. Palmstrøm, and V. S. Pribiag, Nat. Commun. **13**, 5933 (2022).
[20] M. Gupta, G. V. Graziano, M. Pendharkar, J. T. Dong, C. P. Dempsey, C. Palmstrøm, and V. S. Pribiag, Nat. Commun. **14**, 3078 (2023).

[21] R. Mélin and D. Feinberg, Phys. Rev. B **107**, L161405 (2023).
[22] F. Zhang, A. S. Rashid, M. T. Ahari, W. Zhang, K. M. Ananthanarayanan, R. Xiao, G. J. de Coster, M. J. Gilbert, N. Samarth, and M. Kayyalha, Phys. Rev. B **107**, L140503 (2023).
[23] M. Coraiola, D. Z. Haxell, D. Sabonis, H. Weisbrich, A. E. Svetogorov, M. Hinderling, S. C. ten Kate, E. Cheah, F. Krizek, R. Schott, W. Wegscheider, J. C. Cuevas, W. Belzig, and F. Nichele, Nat. Commun. **14**, 6784 (2023).
[24] S. Matsuo, T. Imoto, T. Yokoyama, Y. Sato, T. Lindemann, S. Gronin, G. C. Gardner, S. Nakosai, Y. Tanaka, M. J. Manfra, and S. Tarucha, Nat. Commun. **14**, 8271 (2023).
[25] T. Meng, S. Florens, and P. Simon, Phys. Rev. B **79**, 224521 (2009).
[26] K. Grove-Rasmussen, G. Steffensen, A. Jellinggaard, M. H. Madsen, R. Žitko, J. Paaske, and J. Nygård, Nat. Commun. **9**, 2376 (2018).
[27] M. Žonda, P. Zalom, T. Novotný, G. Loukeris, J. Bätge, and V. Pokorný, Phys. Rev. B **107**, 115407 (2023).
[28] J.-D. Pillet, C. H. L. Quay, P. Morfin, C. Bena, A. L. Yeyati, and P. Joyez, Nat. Phys. **6**, 965 (2010).
[29] D. J. Luitz, F. F. Assaad, T. Novotný, C. Karrasch, and V. Meden, Phys. Rev. Lett. **108**, 227001 (2012).
[30] P. Zalom, Phys. Rev. B **108**, 195123 (2023).
[31] K. Satori, H. Shiba, O. Sakai, and Y. Shimizu, J. Phys. Soc. Jpn. **61**, 3239 (1992).
[32] O. Sakai, Y. Shimizu, H. Shiba, and K. Satori, J. Phys. Soc. Jpn. **62**, 3181 (1993).
[33] M.-S. Choi, M. Lee, K. Kang, and W. Belzig, Phys. Rev. B **70**, 020502(R) (2004).
[34] T. Hecht, A. Weichselbaum, J. von Delft, and R. Bulla, J. Phys. Condens Matter **20**, 275213 (2008).
[35] F. Siano and R. Egger, Phys. Rev. Lett. **93**, 047002 (2004).
[36] F. Siano and R. Egger, Phys. Rev. Lett. **94**, 229702 (2005).
[37] J. E. Gubernatis, *Quantum Monte Carlo Methods: Algorithms for Lattice Models* (Cambridge University Press, New York, NY, 2016).
[38] C. Karrasch, A. Oguri, and V. Meden, Phys. Rev. B **77**, 024517 (2008).
[39] V. Pokorný and M. Žonda, Phys. Rev. B **107**, 155111 (2023).
[40] V. V. Baran, E. J. P. Frost, and J. Paaske, Phys. Rev. B **108**, L220506 (2023).
[41] A. Bargerbos, M. Pita-Vidal, R. Žitko, J. Ávila, L. J. Splitthoff, L. Grünhaupt, J. J. Wesdorp, C. K. Andersen, Y. Liu, L. P. Kouwenhoven, R. Aguado, A. Kou, and B. van Heck, PRX Quantum **3**, 030311 (2022).
[42] L. Pavešič, R. Aguado, and R. Žitko, arXiv:2304.12456.
[43] The mechanism behind both effects is novel and relies on the full phase control over the three-terminal architecture of the device and the presence of Coulomb interactions in the junction region.
[44] P. Zalom, V. Pokorný, and T. Novotný, Phys. Rev. B **103**, 035419 (2021).
[45] See Supplemental Material at http://link.aps.org/supplemental/10.1103/PhysRevLett.132.126505 for details on high-symmetry points and additional data on four-terminal devices, which includes Refs. [46–50].
[46] J. Bauer, A. Oguri, and A. C. Hewson, J. Phys. Condens. Matter **19**, 486211 (2007).
[47] P. Zalom and T. Novotný, Phys. Rev. B **104**, 035437 (2021).
[48] P. Zalom and M. Žonda, Phys. Rev. B **105**, 205412 (2022).
[49] J. C. Estrada Saldaña, A. Vekris, G. Steffensen, R. Žitko, P. Krogstrup, J. Paaske, K. Grove-Rasmussen, and J. Nygård, Phys. Rev. Lett. **121**, 257701 (2018).
[50] R. Žitko, NRG Ljubljana (8f90ac4), Zenodo, 10.5281/zenodo.4841076 (2021).
[51] The dot Green function actually changes, but it has no physical consequences. For a detailed account of this issue for the two-terminal setup, see Ref. [52]. The situation for multiterminal setup is completely analogous.
[52] A. Kadlecová, M. Žonda, and T. Novotný, Phys. Rev. B **95**, 195114 (2017).
[53] The Hamiltonian is invariant under $d_\uparrow \to d_\downarrow$, $d_\downarrow \to d_\uparrow$ followed by a complex conjugation. Note that this antiunitary symmetry is different from time-reversal symmetry attained for two-terminal systems at $\varphi = 0$ as noted in Ref. [42].
[54] The first BZ collapses to 1D in (c) and the green line thus corresponds always to one and the same $\chi = 0$ point.